Available online at www.sciencedirect.com

ScienceDirect

Advances in Space Research 75 (2025) 16–29

ADVANCES IN SPACE RESEARCH (a COSPAR publication)

www.elsevier.com/locate/asr

Spatio-temporal variability of remote sensing reflectance from MODIS imagery for water quality assessment: A case study of Northern Patagonia, Chile

Carlos Lara [a,b], Raúl P. Flores [c], Valentina Córdova [c], Richard Muñoz [a,d], Sebastián I. Vásquez [d,e], Gonzalo S. Saldías [f,g], Iván Pérez-Santos [h,g,i], Antonio Ruíz-Verdú [j], Bernardo R. Broitman [k,l], Amália M.S. Detoni [n,*], Isabel Caballero [m]

[a] Departamento de Ecología, Facultad de Ciencias, Universidad Católica de La Santísima Concepción, Concepción, Chile
[b] Centro de Investigación en Recursos Naturales y Sustentabilidad, Universidad Bernardo O'Higgins, Santiago, Chile
[c] Departamento de Obras Civiles, Universidad Técnica Federico Santa María, Valparaíso, Chile
[d] Programa de Doctorado en Oceanografía, Departamento de Oceanografía, Universidad de Concepción, Concepción, Chile
[e] Instituto de Investigación Pesquera, Talcahuano, Chile, Talcahuano, Chile
[f] Departamento de Física, Facultad de Ciencias, Universidad del Bío-Bío, Concepción, Chile
[g] Centro de Investigación Oceanográfica COPAS Coastal, Universidad de Concepción, Concepción, Chile
[h] Centro I Mar, Universidad de Los Lagos, Puerto Montt, Chile
[i] Centro de Investigaciones en Ecosistemas de la Patagonia (CIEP), Coyhaique, Chile
[j] Image Processing Laboratory, Universitat de València, Paterna, Spain
[k] Departamento de Ciencias, Facultad de Artes Liberales, Universidad Adolfo Ibáñez, Viña del Mar, Chile
[l] Instituto Milenio en Socio-Ecología Costera (SECOS), Santiago, Chile
[m] Instituto de Ciencias Marinas de Andalucía (ICMAN), Consejo Superior de Investigaciones Científicas (CSIC), Puerto Real, Spain
[n] Instituto de Investigaciones Marinas, CSIC, Vigo, Spain

Received 25 June 2024; received in revised form 4 November 2024; accepted 6 November 2024
Available online 13 November 2024

Abstract

The variability of phytoplankton dynamics is a crucial component of coastal biogeochemical cycles at various spatial–temporal scales. A key geophysical parameter that advances our understanding of phytoplankton dynamics in coastal zones is the remote sensing reflectance (R_{rs}), which can be used as a proxy for the concentrations of colored dissolved organic matter (CDOM), phytoplankton biomass, and other organic and inorganic particles. In this work, we used data from the Moderate Resolution Imaging Spectroradiometer onboard the Aqua satellite (MODIS-Aqua) to study long-term trends (2003–2021) in remote sensing reflectance (R_{rs}) across the inner waters of the Chilean northern Patagonia. The Chilean northern Patagonia is a major fjord/channel system receiving large freshwater discharges from continental glacial rivers loaded with terrigenous materials. These discharges significantly alter the water chemistry and its bio-optical properties. Our findings reveal that the optical complexity arising from the interplay between major freshwater sources and the marine system in the Inner Sea of Chiloé leads to a high temporal variability of R_{rs}, primarily linked to the seasonality in turbidity patterns. These findings have significant implications for northern Patagonia's river discharge and turbidity to climate change. They also highlight the substantial changes in water quality (*Chla*, turbidity, etc), triggering shifts in biophysical patterns.

Keywords: Water quality; Ocean color; Temperate regions; Spatio–temporal dynamics

* Corresponding author.
E-mail address: amaliadetoni@gmail.com (A.M.S. Detoni).

https://doi.org/10.1016/j.asr.2024.11.014
0273-1177/

1. Introduction

Over the past 20 years, the continuous monitoring of ocean color has led to unprecedented insights into the spatial and temporal dynamics of phytoplankton biomass (Behrenfeld et al., 2009; Demarcq et al., 2020; Tilstone et al., 2021). The phenology of surface phytoplankton biomass in coastal temperate ecosystems has a well-established sinusoidal variability. Algal cell concentrations are low during winter when light and nutrient supply are limited. Algal blooms occur during spring after solar irradiation increases, and vertical mixing and coastal runoff increase nutrient supply. Bloom senescence occurs when nutrients are depleted through photosynthesis and zooplankton grazing (Sapiano et al., 2012; Friedland et al., 2018; Trombetta et al., 2019). Thus, the seasonal cycle of phytoplankton and the biophysical processes modulating primary production are crucial to understanding coastal biogeochemical cycles (e.g. Hays et al., 2005; Winder and Sommer, 2012; Behrenfeld, 2014).

The spatial and temporal coverage of the satellite ocean color allows us to regionalize *in situ* measurements of phytoplankton abundance or concentration (Gilerson et al., 2022). Several semi-analytical and empirical algorithms have been developed as indicators of phytoplankton biomass (e.g. Blondeau-Patissier et al., 2014; Werther et al., 2022; Yang et al., 2022). Empirical algorithms based on the relationship between *in situ* surface *Chla* and remote sensing measurements vary in complexity, from band ratios and multiple linear regression techniques to machine learning algorithms (Pahlevan et al., 2020; Sherman et al., 2023). Semi-analytical algorithms are linear relationships between inverted remote sensing reflectance (R_{rs}; sr^{-1}) and inherent optical properties (IOPs) of the water. Semi-analytical techniques are used to derive chlorophyll–a (*Chla*) concentrations using the absorption coefficients of other optically active water components independent of the ambient light field (O'Reilly et al., 1998; Sherman et al., 2023). According to the seminal work by Morel and Prieur (1977), IOPs in oceanic waters are dominated primarily by phytoplankton (case I waters). In coastal and inner waters (case II waters), suspended material and non-algal particles introduce uncertainty in the retrieval of *Chla* and water clarity (Liu et al., 2020; McKinna et al., 2021; Turner et al., 2021; Nasiha et al., 2022). A key geophysical parameter for remotely sensed ocean color is R_{rs}, i.e., the ratio of the upwelling radiance to the downwelling irradiance at the ocean surface (Werdell et al., 2018; Dutkiewicz et al., 2019). The different R_{rs} across the ultraviolet (170–380 nm), the visible range (380–780 nm) and near-infrared spectral bands (780–3300 nm) allow us to reduce uncertainties in the size distribution of the different particles that contribute to the IOPs of marine coastal environments (Lee et al., 2007; Doxaran et al., 2007). In this context, it is critical to improve further the performance of bio-optical measurements in aquatic ecology and water quality studies in coastal and inner waters (Wei et al., 2018; Bisson et al., 2021).

In northern Patagonia (41–45°S), the transition from pristine temperate rainforests to landscapes modified by agriculture and timber plantations changes the quality of freshwater in streams and rivers (León-Muñoz et al., 2013). The significant input of terrestrial organic carbon can alter the supply of mineralized nutrients and other solids, influencing the penetration of light into the water column, hence the structure of autotrophic biomass (González et al., 2010; Cuevas et al., 2019). Northern Patagonia is a major fjord–channel system that receives large freshwater discharges from continental glacial rivers (Lara et al., 2016; Flores et al., 2022) loaded with terrigenous substances (e.g., colored dissolved organic matter; CDOM) that modify the chemistry, bio-optical properties of coastal waters (Curra-Sánchez et al., 2022), and nutrient ratios (e.g., Si: N or Si: P) on multiple temporal and spatial scales (Vargas et al., 2011; León-Muñoz et al., 2021). Similarly, the meridional pattern in biological activity exhibits high variability in response to annual variation in environmental forcing (Lara et al., 2016; Vásquez et al., 2021; Muñoz et al., 2023). High-resolution satellite products can aid in evaluating the status of autotrophic by-products and assess potential changes in water quality in northern Patagonia. To date, most studies in northern Patagonia have focused on the variability of freshwater input from rivers (Flores et al., 2022), the evolution of sea surface temperature (SST) and salinity fronts (Saldías et al., 2021), among other characteristics of ocean color (e.g. Lara et al., 2016; Vásquez et al., 2021; Muñoz et al., 2023) on multiple spatio-temporal scales.

In this study, we evaluated the variability of the R_{rs} and band ratios derived from the MODIS–Aqua sensor to investigate seasonal variations in water quality in northern Patagonia. We aim to comprehensively examine the trends of R_{rs} in visible wavelengths (412–678 nm) for surface waters of the Inner Sea of Chiloé (ISC) in northern Patagonia during the MODIS-Aqua period (2003–2021). These analyses contribute novel insights to enhance biogeochemical monitoring and refine modeling efforts within this bio-optically poorly studied region. This study focuses on elucidating patterns of bio-optical properties of water, which are crucial for capturing the pronounced spatial and temporal variability observed within the area.

2. Materials and methods

2.1. Study area

The ISC is located in northern Patagonia and is characterized by the presence of several oceanographic basins (see

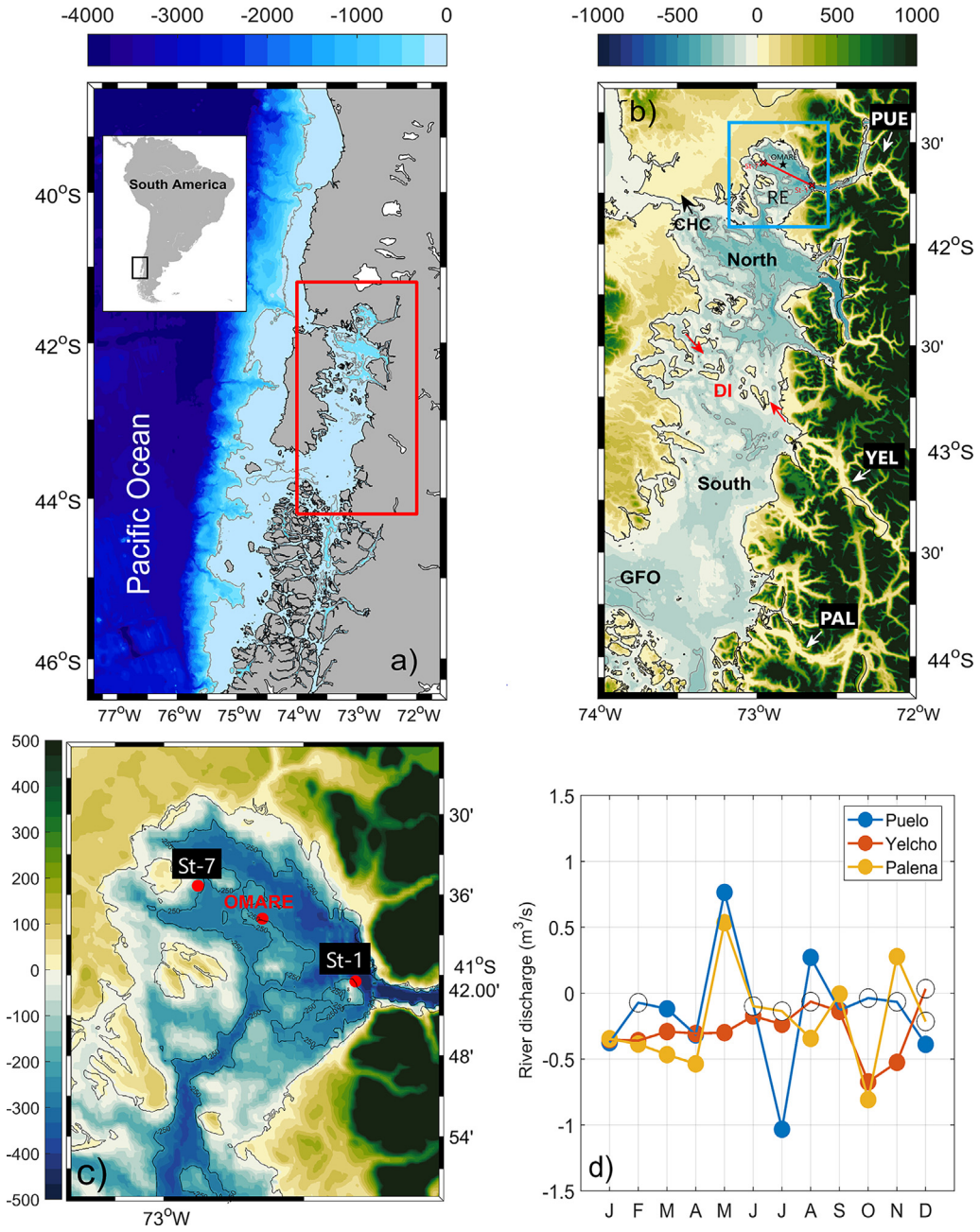

Fig. 1. (a) Bathymetry of south-central Chile. The red box show of the study area. (b) Inner Sea of Chiloé. GFO: Boca del Guafo, CHC: Chacao channel, PUE: Puelo River, YEL: Yelcho River, PAL: Palena River and, DI: Desertores Island, RE: Reloncaví estuary. (c) Longitudinal section from station St-1 to St-7. d) trend river discharge (2001–2020. The filled circles show those months that are significant in the trend (p-value<0.05). The color bar show the depth (in meters) and the solid gray line in a) and b) panels the 200 m isobath. Bathymetric data were obtained from The General Bathymetric Chart of the Oceans GEBCO (https://www.gebco.net/) and river discharge of the Dirección General de Aguas, DGA (https://dga.mop.gob.cl/Paginas/hidrolin.easatel.aspx).

Fig. 1) exhibiting high heterogeneity in local environmental conditions (Iriarte et al., 2007; Vásquez et al., 2021; Saldías et al., 2021). The precipitation and streamflow regimes have shown a marked decrease in magnitude in the past decade compared to historical averages (Aguayo et al., 2021), which has had repercussions on the seasonal variation in the structure of autotrophic communities (González et al., 2010; Iriarte et al., 2017) and the biogeochemical processes therein (Linford et al., 2023). The marine system along the ISC is influenced by the intrusion of high-salinity oceanic waters through the Chacao Channel (CHC) from the north and Boca del Guafo from the south (see CHC and GFO, Fig. 1(b)) (Strub et al., 2019; Vásquez et al., 2021). Large freshwater inputs enter from several continental rivers, mainly (from north to south) Puelo, Yelcho and Palena (see PUE, YEL and PAL, Fig. 1(b)). Small rivers also drain into the ISC from Chiloé island; several do so through the densely urbanized Castro fjord area, at the

west end of the Desertores island chain, and facing the Yelcho drainage on the continental side (Fig. 1(b)). To explore the long term variability in R_{rs}, we separated the ISC into two sub-regions based on *SST* and $Chl-a$ regimes (Lara et al., 2016; Saldías et al., 2021) (42.6°S, see red arrows in Fig. 1(b)).

2.2. Satellite and processing data

To study long-term trends in R_{rs} from January 2003 to December 2021, we used quality-controlled daily swaths create gridded monthly composites at a spatial resolution of 1000 meters. We downloaded the level-2 imagery from MODIS–Aqua from NASA's Ocean Color website (http://oceancolor.gsfc.nasa.gov). MODIS–Aqua is a polar-orbiting NASA Earth Observation satellite, local ascending at the equator, with a 1:30 pm local standard time overpass. The MODIS–Aqua sensor has ocean bands (bands 8–14) with high gain settings to sense the characteristics of dark water bodies. In contrast, the land bands used here (bands 1, 3, 4) have lower gain settings to detect brighter features on land, which can be used in brighter inland and coastal water bodies (Franz et al., 2006). After an atmospheric correction to remove the contributions of aerosols and additional corrections for whitecaps, sun glint, and other artifacts, ocean water contributes less than 10% of the top-of-atmophere (TOA) reflectance (Katsaros, 2015). Using corrected TOA data, we calculated R_{rs} at the water surface with the 10 bands that are useful for ocean color studies: 412, 443, 469, 488, 531, 547, 555, 645, 667, and 678 nm (Ahmad et al., 2010; Feldman and McClain, 2014). A variable number of images were used each year from 2003 to 2021, specifically: 817, 819, 812, 805, 795, 809, 804, 804, 811, 799, 799, 797, 803, 802, 797, 803, 793, 769, and 788. All data were processed using Matlab 2017b (The MathWorks Inc, 2017).

2.3. River discharge and in situ hydrographic data

Daily (2001–2020) discharge data for the Puelo, Yelcho, and Palena rivers were obtained from their respective monitoring station from the Sistema Hidrométrico en Línea of Dirección General de Aguas, Chile (https://dga.mop.gob.cl/Paginas/hidrolineasatel.aspx). The Servicio Hidrométrico Nacional has 1330 stations that transmit online data through the satellite systems or GPRS (General Packet Radio Service). The locations of the selected monitoring stations are indicated in Fig. 1b. Daily flow measurements were averaged monthly and the months that showed statistical significance p-value <0.05 in the river flow trend were identified.

In order to establish seasonal variability and surface spatial distribution (1 m depth) of turbidity and *Chla* in coastal waters, we carried out two oceanographic cruises in austral summer (January 22) and winter (July 27) in 2021. All cruises included a towed longitudinal section from station St-1 to St-7 (see Fig. 1c) using an AML–3 XC profiler (AML Oceanographic, Canadá). This instrument can be submerged to 600 m and has auxiliary dissolved oxygen, turbidity, and *Chla* sensors. The auxiliary turbidity sensor is provided by X2change^{TM} Sensors with a maximum profiling depth of 600 m. The measurement range varies between 0–3000 NTU with a resolution of 0.01 NTU and a response time <0.7 s. The auxiliary *Chla* sensor has a measurement range between 0–500 ug/L with a resolution of 0.01 ug/L and a response time of 200 ms. Using the turbidity and *Chla* data from the cruises, surface sections were constructed to analyze the spatial variability of both variables. Finally, we obtained *in situ* hourly turbidity and *Chla* (1 m depth) data from the OMARE hydrographic buoy for the 2018–2023 period from Centro de Estudios Avanzados en Zonas Áridas (CEAZA-Met, https://www.ceazamet.cl/).The maintenance is regularly carried out by Centro i-mar, Universidad de Los Lagos, Chile (see location in Fig. 1).

2.4. Climatology and trends

For the calculation of climatologies and trends, we divided the ISC into northern and southern marine basins along the axis of the Desertores Islands (e.g., Lara et al., 2016). The monthly gridded data for all pixels in each region was then averaged to obtain univariate time series for each R_{rs} band. We computed the band ratios of individual bands as $R_{rs}(\lambda_1)/R_{rs}(\lambda_2)$, where $\lambda_1 < \lambda_2$ (e.g., Turner et al., 2021). Spatially averaged R_{rs} data were used to compute climatologies and trends for the individual univariate $R_{rs}(\lambda)$ bands and the band ratios ($R_{rs}(\lambda_1)/R_{rs}(\lambda_2)$). In addition, we generated spatial maps of long-term trends by computing trends for individual pixels. The climatologies were used to identify patterns of seasonal variability in space. Long-term trends were calculated using the slope of a least-squares fit. The statistical significance was evaluated by their p value, using 90% confidence ($p < 0.1$) intervals. Following Turner et al. (2021), trends were expressed in terms of relative change using the trend per year normalized by the long-term mean value:

$$Relative\ change(\%yr^{-1}) = \frac{trend_{Rrs}(sr^{-1}yr^{-1})}{mean_{Rrs}(sr^{-1})} \quad (1)$$

$$Relative\ change(\%yr^{-1}) = \frac{trend_{\frac{Rrs(\lambda_1)}{Rrs(\lambda_2)}}(sr^{-1}yr^{-1})}{mean_{\frac{Rrs(\lambda_1)}{Rrs(\lambda_2)}}(sr^{-1})} \quad (2)$$

3. Results

3.1. Temporal variability in mean monthly R_{rs}

In general, temporal trends in all R_{rs} and band ratios evidenced a spatially homogeneous positive trend for the ISC (see Supplementary Figs. 1 and 2). The climatology of the individual R_{rs} bands showed high temporal heterogeneity (Fig. 2. In the blue spectral region, the maximum values

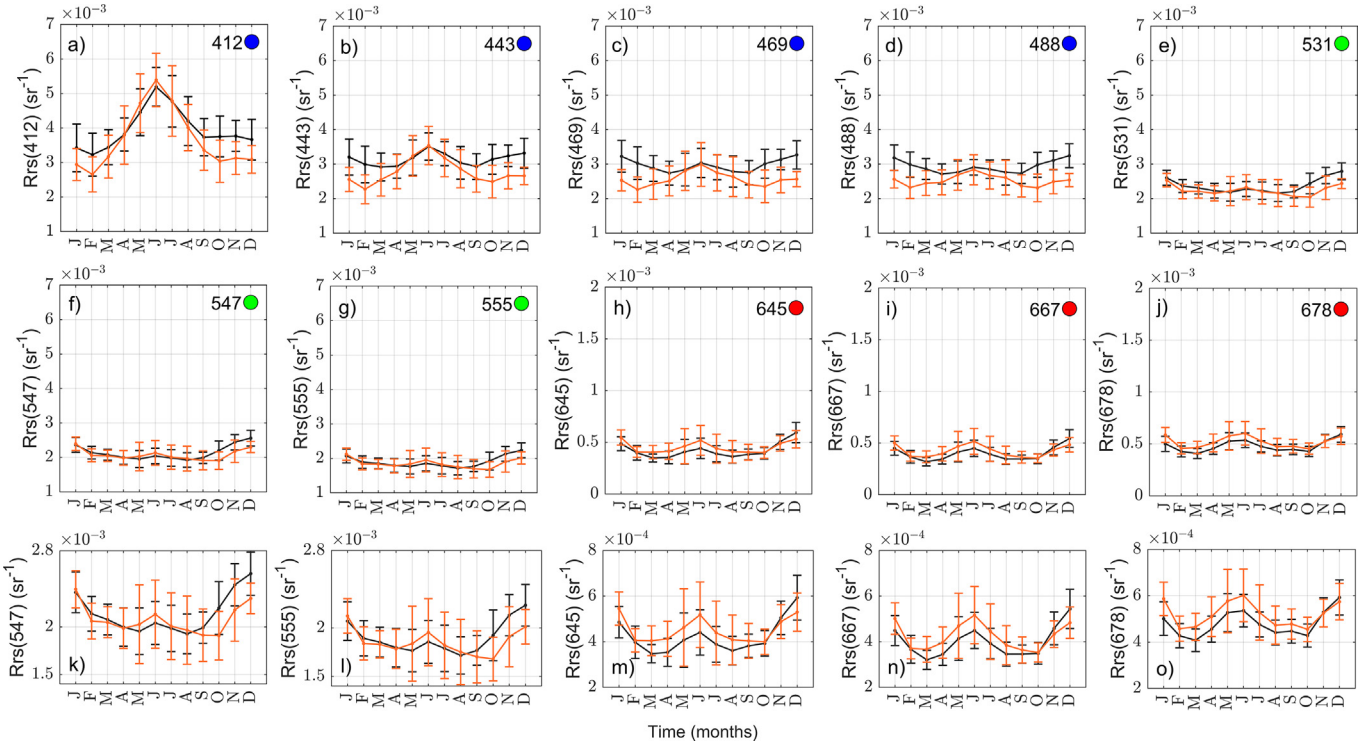

Fig. 2. Climatology of mean monthly R_{rs} for each MODIS band over the 2003–2021 period. R_{rs} series have been averaged over the northern (black) and southern (orange) ISC, as defined in Fig. 1. Error bars represent the standard deviation of the region-averaged R_{rs} series over the same time period. By wavelenght, climatologies show (a) $R_{rs}412$, (b) $R_{rs}443$, (c) $R_{rs}469$, (d) $R_{rs}448$, (e) $R_{rs}531$, (f) $R_{rs}547$, (g) $R_{rs}555$, (h) $R_{rs}645$, (i) $R_{rs}667$, (j) $R_{rs}678$. Panels k–o correspond to zoomed-in versions of panels f–.j, respectively.

(sr^{-1}) were observed between May and July (Fig. 2)) between November and January (Fig. 2(c,d)), while the lowest values occurred during the austral summer. The 412 nm band showed the highest values, which were accompanied by a high standard deviation (Fig. 2(a)). The bands corresponding to the green spectral region (i.e., 531, 547, and 555 nm, respectively) generally showed lower spatial variability in their average values and standard deviations compared to reflectance in the blue spectral region (Fig. 2(e-g)). The spectral bands associated with the red spectral region exhibited higher temporal variability and standard deviations than those observed in the green region; however, these values were the lowest among all R_{rs} observations ($< 1x10^{-3} sr^{-1}$). When examining the red/-green climatological ratios, high homogeneity and low standard deviation were observed in both the northern and southern regions (Fig. 3(a-g)). The greatest temporal variability was observed in the green/blue ratios in association with high standard deviations (Fig. 3(i-k)); these ratios also showed higher magnitudes in the northern region of the ISC. Climatologically, the green/red band ratios exhibited the highest values during December and January, while the highest green/blue band ratios were observed between February and April. Interestingly, the $R_{rs}488/R_{rs}469$ ratio (Fig. 3l) showed low spatial and temporal heterogeneity, with values around 1–1.5. It is important to note that the climatology of all R_{rs} for the northern region had higher values than the southern region throughout the spectral range examined here.

3.2. Spatial heterogeneity in mean monthly R_{rs}

Single R_{rs} bands showed significant spatial heterogeneity along the ISC (in terms of northern and southern regions). The $R_{rs}412, R_{rs}443$ and $R_{rs}488$ showed significant negative trends in the Reloncaví Sound, an area directly influenced by the Puelo River (Fig. 4 (a-d)). In contrast, the blue $R_{rs}469$ band showed a negative overall trend along the ISC. The green bands $R_{rs}531, R_{rs}547$, and $R_{rs}555$ also exhibited a significant and negative trend at the eastern boundary of the Reloncaví Sound and, generally, around the mouths of major rivers (Fig. 4(e-g)). Disagreeing with this general spatial pattern, the red bands $R_{rs}645$ and $R_{rs}667$ (Fig. 4(h-i)) showed a positive and significant trend in the western band of the northern region of ISC. In contrast, the $R_{rs}678$ band showed a significant negative trend spanning the axis of the Desertores Islands (Fig. 4j). As evidenced in Fig. 5, the red and green band ratios did not show significant spatial trends at a 95% confidence level except for small areas close to the coast along the northern sector (Fig. 5(a-h)). In contrast, the spatial heterogeneity between the green and blue band ratios revealed a spatially

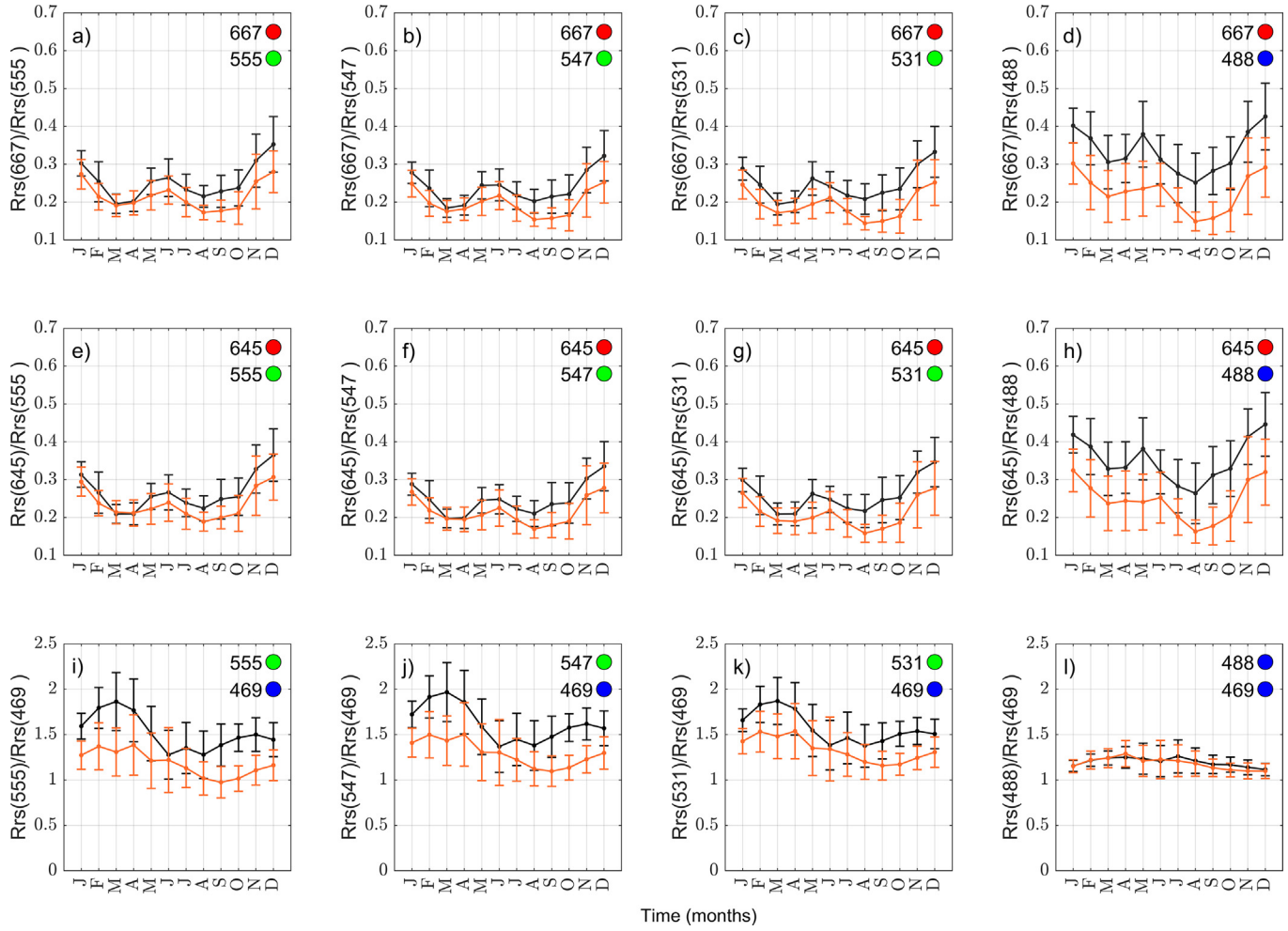

Fig. 3. Climatology for R_{rs} ratios for the 2003–2021 period. R_{rs} ratios series have been averaged over northern (black) and southern (orange) ISC, as defined in Fig. 1. Error bars represent the standard deviation of the region-averaged R_{rs} series over the same time period. By wavelenght, climatologies show (a) $R_{rs}667/R_{rs}555$, (b) $R_{rs}667/R_{rs}547$, (c) $R_{rs}667/R_{rs}531$, (d) $R_{rs}667/R_{rs}488$, (e) $R_{rs}645/R_{rs}555$, (f) $R_{rs}645/R_{rs}547$, (g) $R_{rs}645/R_{rs}531$, (h) $R_{rs}645/R_{rs}488$, (i) $R_{rs}555/R_{rs}469$, (j) $R_{rs}547/R_{rs}469$, (k) $R_{rs}531/R_{rs}469$, (l) $R_{rs}469/R_{rs}488$.

extensive and significantly increasing trend, which, in the case of the blue/blue band ratio encompassed almost the entire study area (Fig. 5i-l).

3.3. Trends in mean monthly R_{rs}

In general, the seasonality trends for single bands did not show significant differences between regions during the austral summer months (December, January, and February Fig. 6). However, the northern region generally exhibited a pattern of greater variability in monthly trends for all R_{rs} bands. Blue bands exhibited statistically significant and synchronous trends between May-June and October (austral late fall-early winter and spring, respectively) in both ISC regions (Fig. 6a-d). Interestingly, $R_{rs}412$ showed a positive trend in late austral winter (August), while $R_{rs}443$ and $R_{rs}469$ showed the opposite pattern during the preceding months (May, June, July), for the north and the south ISC, respectively. We did not detect any significant trends in reflectances for any of the green bands ($R_{rs}531$ to $R_{rs}555$). In the case of the red R_{rs} bands, we found significant negative trends during late austral spring in the southern region (November, Fig. 6h-j). We found significant area-averaged trends for all band ratios examined, and patterns sometimes differed between ISC regions (Fig. 7). Again, greater temporal variability was evident in the northern region except for the green/blue and blue/blue ratios. Across all the red/green and red/blue ratios, trends for late austral spring (November) were significantly negative and only for the southern basin (Fig. 7a-h). Based on the green/blue ratios, our findings reveal significant positive trends synchronous between regions only during austral fall (May-June). On the other hand, the southern region showed significant positive trends for all green–blue ratios for late austral fall (May-July) or widespread positive trends from austral fall to spring (October, Fig. 7i-k). Finally, the $R_{rs}488/R_{rs}469$ band ratio showed a significant positive trend almost year-round in both regions (Fig. 7l).

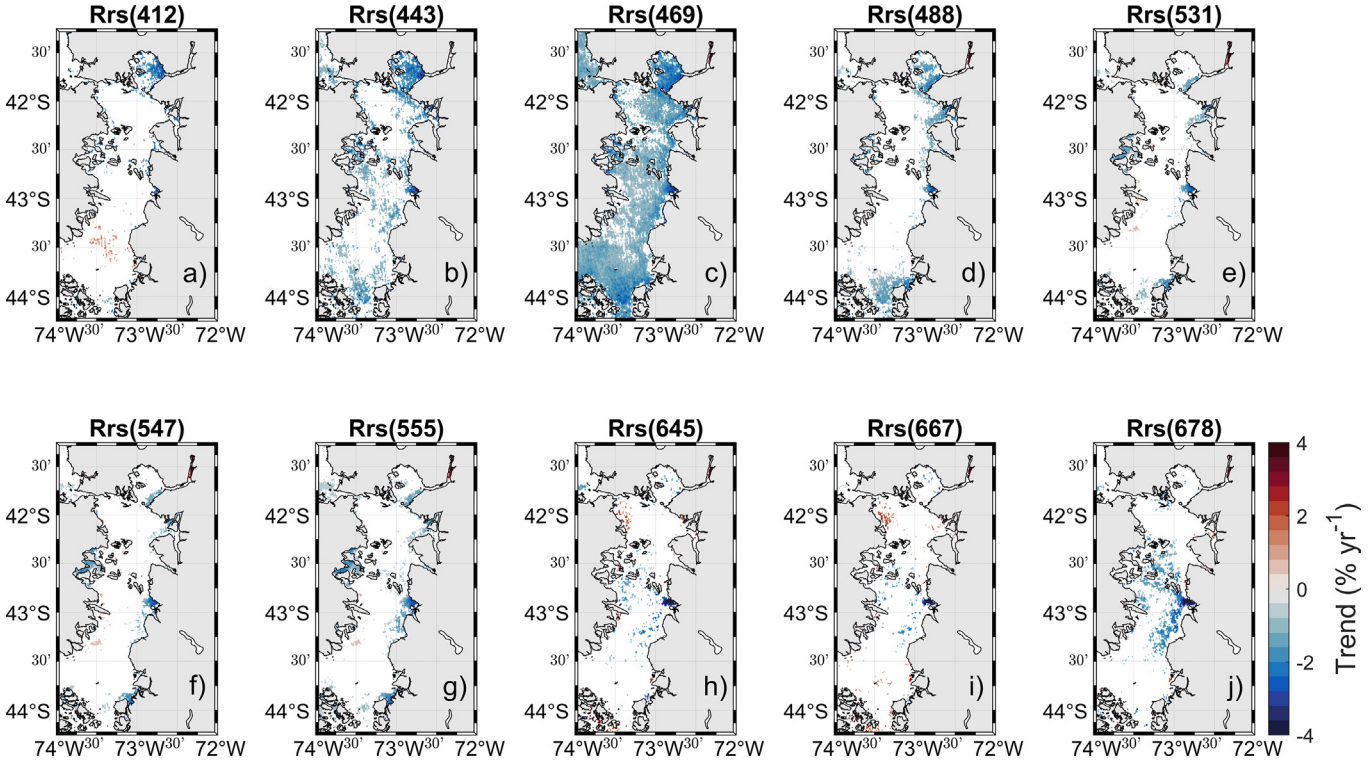

Fig. 4. Significant trends ($p < 0.1$) over time in R_{rs} at single bands, from 2003–2021 for (a) $R_{rs}412$, (b) $R_{rs}443$, (c) $R_{rs}469$, (d) $R_{rs}488$, (e) $R_{rs}531$, (f) $R_{rs}547$, (g) $R_{rs}555$, (h) $R_{rs}645$, (i) $R_{rs}667$, (j) $R_{rs}678$. Trends are expressed as relative trends normalized to the long-term mean R_{rs} at each location.

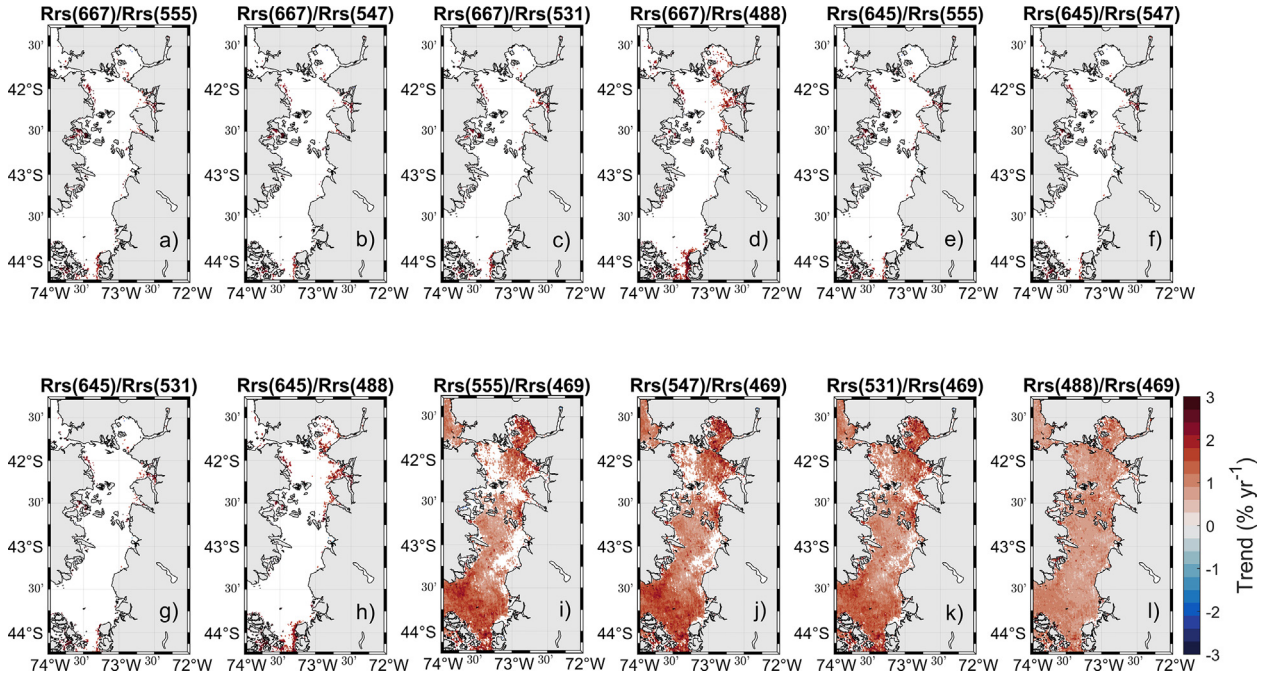

Fig. 5. Significant trends ($p < 0.1$) over time for R_{rs} ratios for the 2003–2021 period. (a) $R_{rs}667/R_{rs}555$, (b) $R_{rs}667/R_{rs}547$, (c) $R_{rs}667/R_{rs}531$, (d) $R_{rs}667/R_{rs}488$, (e) $R_{rs}645/R_{rs}555$, (f) $R_{rs}645/R_{rs}547$, (g) $R_{rs}645/R_{rs}531$, (h) $R_{rs}645/R_{rs}488$, (i) $R_{rs}555/R_{rs}469$, (j) $R_{rs}547/R_{rs}469$, (k) $R_{rs}531/R_{rs}469$, (l) $R_{rs}488/R_{rs}469$.

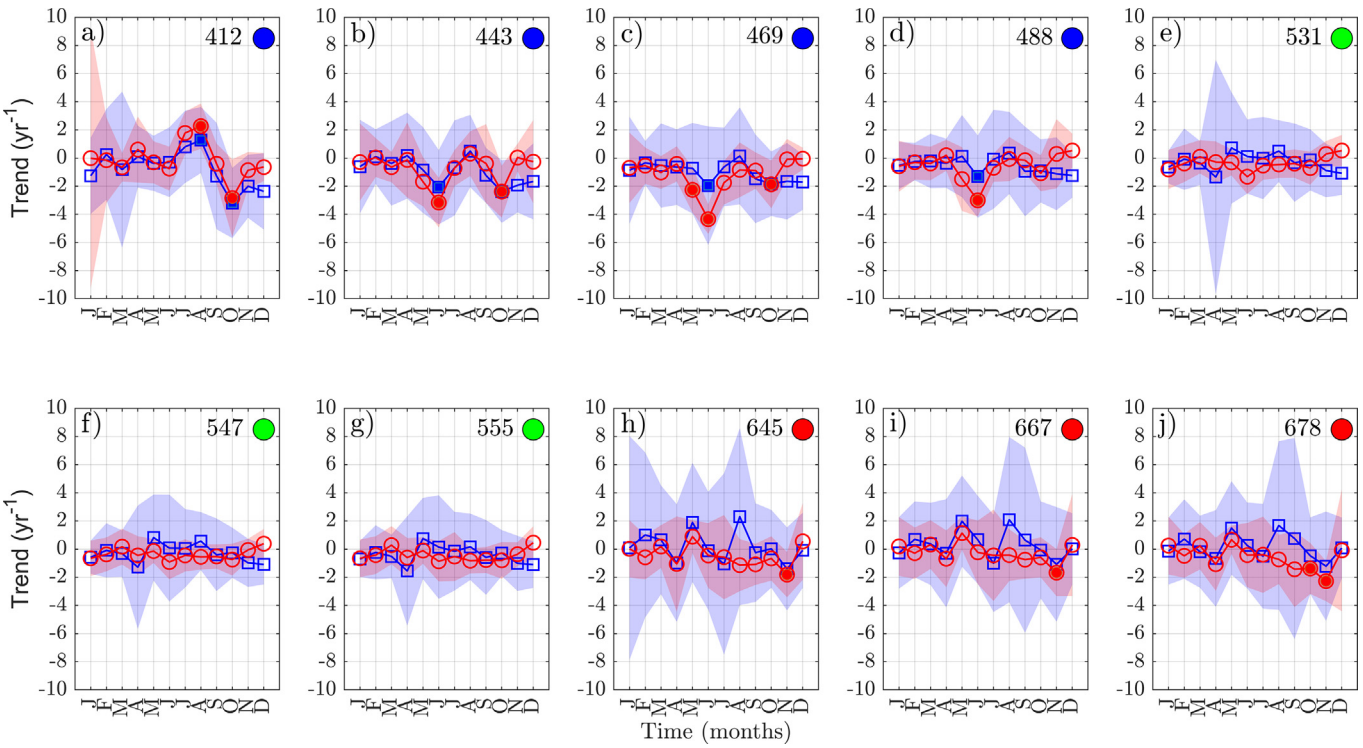

Fig. 6. Climatology of trends over time for each R_{rs} band for the 2003–2021 period. Blue circles indicate mean trends for the northern and red squares indicate mean trends for the southern ISC, as defined in Fig. 1. The shaded areas indicate the spatially-averaged standard deviation for the trends in each region. Filled symbols indicate significant trends.

3.4. Temporal variability of in situ turbidity

The climatological analysis identified two prominent annual peaks in turbidity levels: the first in April (austral fall) with an average value of 0.33 NTU and the second in November (late austral spring) with an average value higher than the first peak in April (1.33 NTU). The lowest turbidity was identified in June and July with values of 0.03 and 0.04 NTU, respectively (Fig. 8a). The *Chla* climatology showed a first peak in April (4.1 ug/L) and a second peak in August of lower magnitude (3.2 ug/L). May, July, and November showed the lowest *Chla* concentrations with values < 1.3 ug/L (Fig. 8b). In general, the monthly variability of turbidity is well related to *Chla* where turbidity peaks are inversely proportional to *Chla* peaks (i.e. in November).

Turbidity and *Chla* were collected in surface waters along a zonal section (St-1 to St-7) during two campaigns conducted in 2021 with St-1 situated near the eastern shore at the Puelo River mouth and the St-7 near the opposite shore (western shore).The sections of turbidity and *Chla* showed differences and between the seasons of Juny and July. The tubidity in January showed average values of 0.53 ± 0.12 NTU while, in July the turbidity was 0.48 ± 0.08 NTU. In space, the January towed section of turbidity showed greater variability than in July at the mouth of the Puelo River (St-1) which was more noticeable after the OMARE buoy towards St-7 (Fig. 8c). The surface sections of *Chla* revealed a strong contrast between the months of January and July with average values of 1.30 ± 0.29 and 5.67 ± 3.78 ug/L, respectively. As with turbidity, the position of the OMARE buoy marks a longitudinal boundary between low (before) and high (after) *Chla* (Fig. 8d).

4. Discussion

Our results provide the first regional-scale evaluation of remote sensing reflectances (R_{rs}). Results are consistent with seasonal patterns found in some of the satellite characteristics (e.g. *Chla*, SST, river plumes) described for temperate zones (Iriarte et al., 2007; Vásquez et al., 2021; Flores et al., 2022; Muñoz et al., 2023), and have important implications for the study of water quality in case II waters (inland and coastal ocean waters) (Blondeau-Patissier et al., 2014; Dogliotti et al., 2015; Turner et al., 2021). However, some aspects of this study require special attention. Remote sensing-derived reflectances R_{rs} are useful to monitor and retrieve water quality parameters in the upper ocean layer as their optical properties depend on phytoplankton abundance and composition, the concentrations of suspended matter (sediments and detritus), and dissolved organic matter (Hellweger et al., 2004; Yang et al., 2022).

Over the last 20 years, with advances in remote sensing technologies, different bio-optical algorithms have been developed to estimate water quality variables with high precision and low bias (Doxaran et al., 2007; Topp et al.,

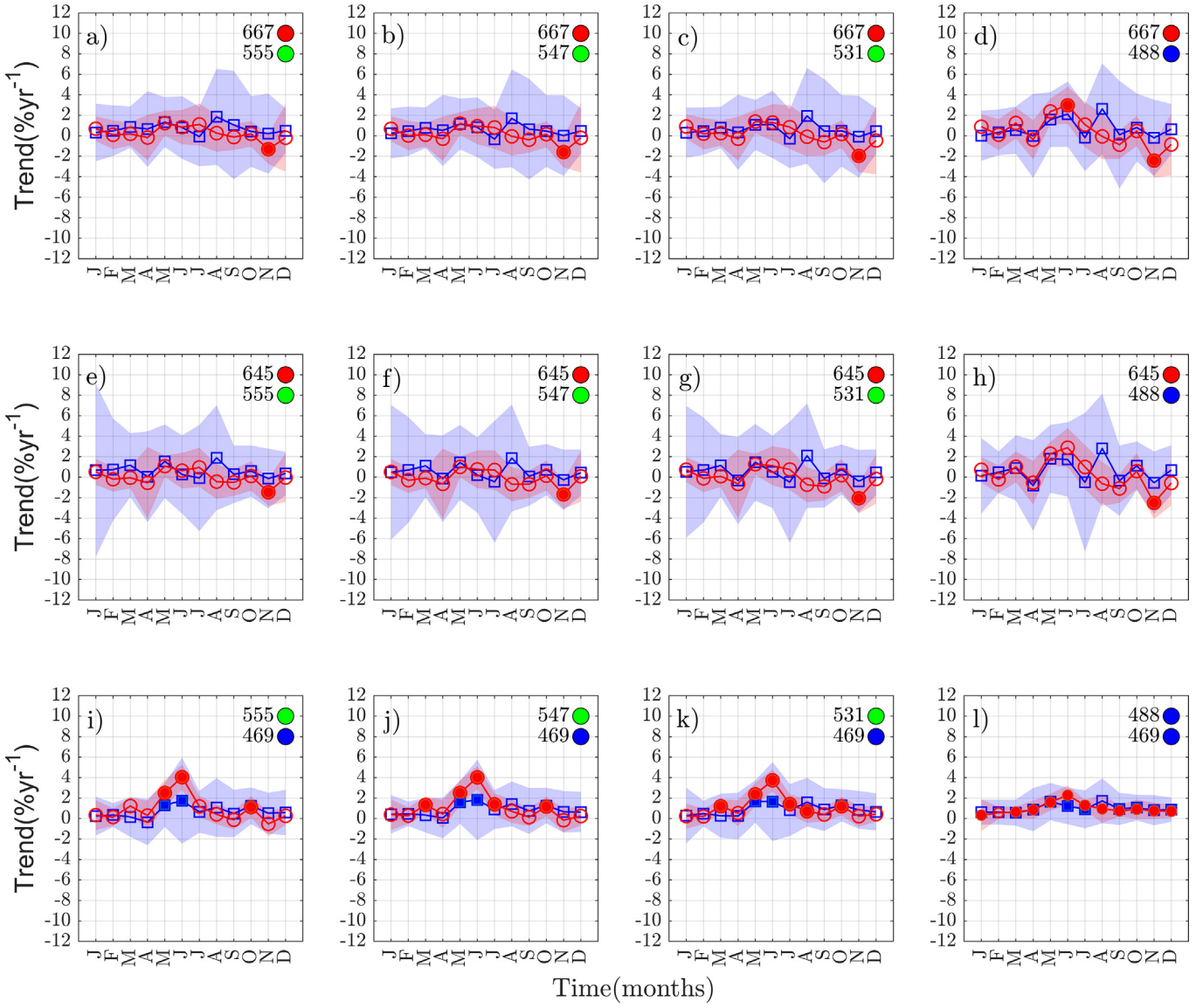

Fig. 7. Climatology of trends over time for R_{rs} ratios for the 2003–2021 period. Blue circles indicate mean trends for northern ISC and red squares indicate mean trends for southern ISC, as defined in Fig. 1. The shaded areas indicate the spatially-averaged standard deviation for the trends in each region. Filled symbols indicate significant trends.

2020). The optical characteristics of *Chla* have been established in different ecosystems (ocean, lakes, inland waters) and then used as a proxy of biological activity to study patterns of spatio-temporal variability (Saberioon et al., 2020; Vásquez et al., 2021; Karimi et al., 2024). However, the optical complexity of the interaction between rivers and marine systems has received limited attention. Optical properties are strongly influenced by time-varying processes such as river runoff and snowmelt. In this way, the optical complexity associated with turbid freshwater has curtailed the use of satellite data to characterize the temporal dynamics in these region (Flores et al., 2022; Curra-Sánchez et al., 2022). The seasonality in autotrophic biomass along the ISC is often related to the seasonality of river outflow, sea surface temperature and solar radiation (Iriarte et al., 2007; González et al., 2010). Satellite retrieval of algal pigments (such as *Chla*) as an index of the productivity of marine ecosystems is often based on blue, green, or near-infrared (Blondeau-Patissier et al., 2014). In case II waters, the absorbance of the humic color (referred to here as colored dissolved organic matter, CDOM), more specifically in the blue region (412 and 443 mn), is higher than for *Chla* (Menken et al., 2006), affecting the accuracy of surface *Chla* estimates in some coastal ecosystems (Mishra and Mishra, 2012).

In this study, we noted a higher band ratios values in northern basin, comparing with southern basin. According to our observations, this is primarily due to the northern basin being influenced by greater river discharges, especially during the austral fall and spring seasons, when the highest precipitation (fall) and river input (spring) occurs (Lara et al., 2016; León-Muñoz et al., 2021). Additionally,

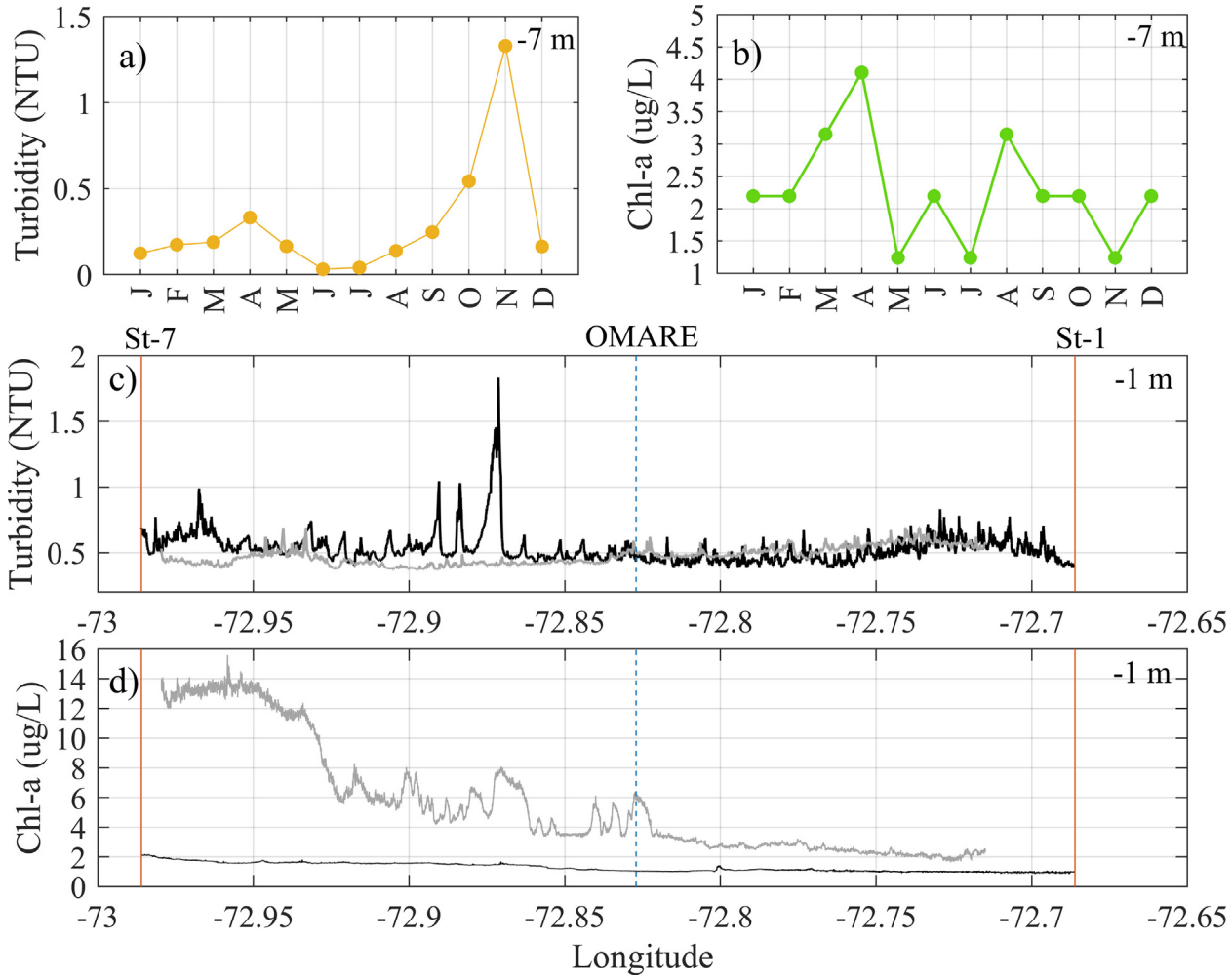

Fig. 8. a) Annual climatology for turbidity and b) chlorophyll-a (2018–2023) at −1 m. Longitudinal Section (1 m depth) for c) turbidity and d) chlorophyll-a in 22, January (black line) and 27, July, 2021 (gray line) in 2021. The St–7 near to river discharge and ST-1 marine condition.

factors such as harmful algal blooms and autochthonous organic particles and allochthonous particulate organic carbon from rivers or glaciers that enhances a diverse particle pool (Vargas et al., 2011) may introduce greater variability in the northern basin (García-Tuñon et al., 2024). Flores et al. (2022) conducted an EOF analysis of $R_{rs}645$, revealing spatial differences among the first three modes for the northern and southern basins. Furthermore, Muñoz et al. (2023) identified spatial differences in the first two EOF modes between the northern and southern basins for *Chla*, which influence the biophysical properties of the study area. This consideration is relevant to improving our interpretation of R_{rs} bands and their contribution to understanding the biophysical dynamics in the ISC. Indeed, this is critical to define relevant IOPs in optically complex waters (Lo Prejato et al., 2020).

We detected significant decreasing trends in the blue part of the spectrum during early winter and spring, and spatio-temporal trends were apparent for $R_{rs}469$. The reduced reflectance and hightened absorption at 469 nm, a characteristic wavelength associated with the absorption spectrum of carotenoid xanthophylls, crucial for photoprotection (Roy et al., 2011). Notably, pigments like canthaxanthin, dinoxanthin, and violaxanthin constitute these xanthophylls, exhibiting high absorption coefficients around 469 nm (Roy et al., 2011). These pigments are integral to the pigment profiles of potentially harmful red tide-forming dinoflagellates, including *Karenia spp.*, *Alexandrium minutum*, *lexandrium minutum*, *Gymnodinium catenatum*, and *Dinophysis spp* (Gong et al., 2017).

Turbidity, a commonly used physical parameter for assessing the optical environment for water quality, exhibits spatio-temporal variations alongside those observed for *Chla*, such that observations of *Chla* typically aid in identifying areas at risk of elevated turbidity (Cloern, 1987). Understanding turbidity as a measure of the amount of light scattered and absorbed by different components of the water column is crucial for effective water resource management and ecosystem productivity control (Wang et al., 2019, and references therein). Surface turbidity is generally determined by sediment resuspension in shallow or coastal areas or transport from terrestrial systems (Cloern, 1987). The climatological analysis to *in situ* turbidity (Fig. 8a) at 1 m depth reveals lower turbidity values in

austral winter (June and July) and summer (January). These findings indicate that decreased turbidity in July 2021 (longitudinal section) facilitated enhanced light penetration into the water column, promoting increased phytoplankton biomass during that year. The significant p-values ($p \leqslant 0.05$) observed between *in situ* turbidity and R_{rs} bands used in this study (Table 1) show consistency with the significant trends, particularly those found in the closest region of the electromagnetic spectrum (i.e., blue and green). This could be attributed to the seasonality of the CDOM input (high absorption in the blue bands) resulting from riverine inputs (González et al., 2010; Curra-Sánchez et al., 2022) and the elevated *Chla* concentrations (high reflectance in the green bands) in the region, especially during the austral spring-summer seasons (Iriarte et al., 2007; González et al., 2010; Vásquez et al., 2021).

Seasonal peaks of high turbidity (1 m depth) were observed during spring (October and November) (Fig. 8a), which coincides with increased river discharge deliver freshwater and sediments in the study region (Wetz et al., 2006; Flores et al., 2022). The spatial variability of turbidity and *Chla* was high between months and along the longitudinal section. Average turbidity values were higher in January (0.53 NTU) and lower in July (0.48 NTU), while *Chla* showed higher average values in July (5.67 μg/L) and lower values in January (1.30 μg/L). This pattern is consistent with inland waters characterized by high turbidity from continental inputs or sediment resuspension leading to low phytoplankton production due to limited light availability (González et al., 2019). Phytoplankton dynamics, including productivity and spatial/temporal changes in biomass, are primarily governed by light (Cloern, 1987; Wang et al., 2019). Zonal variability in turbidity and *Chla*, associated with seasonal river discharges (see Fig. 1d), generates freshwater plumes with high levels of biological activity in austral spring. This is coherent with a high probability of SST fronts associated with the Puelo River discharge (Saldías et al., 2021). The climatology of turbidity at 1 m depth is consistent with the monthly variability of the longitudinal sections with higher turbidity values in January compared to July. On the other hand, the climatology of *Chla* showed higher concentrations in January and lower ones in July in contrast to that reported by the longitudinal sections where surface *Chla* measurements (1 m depth) in July were higher compared to January. The differences in *Chla* in the climatology and in the towed sections may result from the differences in the depth of the sensors and the quality of the "photosynthetically active light" received by the phytoplanktonic organisms at the surface and subsurface, highlighting the importance of depth in the measurements and the role played by the biological factor in the variability of *Chla* (Morel and Berthon, 1989; Mann and Lazier, 2005).

Finally, and given that the primary source of CDOM is allochthonous, i.e., originates primarily from terrestrial inputs subsidies from outflow river (Cannizzaro et al., 2013; Curra-Sánchez et al., 2022), it is essential to establish a baseline, from a remote sensing perspective, which are the bandwidths at which these main water components modify the IOPs in case II waters (Shi and Wang, 2019). Turbidity measurements have been assessed through remote sensing studies using the red and NIR bands, which are also widely used in developing algorithms for estimating surface *Chla* in turbid waters (Chen et al., 2007, and references therein; Nechad et al., 2009; Constantin et al., 2016; Cui et al., 2020). Consequently, a correlation between these two parameters is expected. However, turbidity is an indirect measure of multiple optically active constituents (OACs), including dissolved (e.g. CDOM, suspended sediments, phytoplankton,) and particulate (mostly inorganic) matter, which optically competes with *Chla* (Chen et al., 2007; Constantin et al., 2016). In most inland, estuarine, and coastal (case II) waters, the overlapping and uncorrelated absorption by OACs in key spectral regions (e.g blue and green) can greatly bias retrievals of *Chla* (Gitelson et al., 2009; Gitelson et al., 2011). Moreover, various physical and biological processes operate to resuspend bottom sediments over multiple temporal scales. The amount of solids in suspension in the water column also changes the OACs in the water column and also alters the size-distribution of particulate matter, thereby affecting the absorption and scattering per unit mass of suspended solids (Menon and Adhikari, 2018; Laiolo et al., 2021). Hence, it is crucial to identify the spectral signatures of these OSCs within optically complex marine systems.

Table 1
Pearson's Correlation (R^2), significance at $^{*}p \leqslant 0.05$ and root mean square error (RSME) between *in situ* turbidity and each R_{rs} bands used in this study for period 2018–2020.

Wavelength	Color	R^2	p-value	RMSE
Rrs_{412}	Blue	0.58	0.10	2.1542e + 3
Rrs_{443}	Blue	0.94	0.01*	2.1542e + 3
Rrs_{469}	Blue	0.86	0.03*	2.1542e + 3
Rrs_{488}	Blue	0.81	0.04*	2.1542e + 3
Rrs_{531}	Green	0.91	0.02*	2.1542e + 3
Rrs_{547}	Green	0.89	0.02*	2.1541e + 3
Rrs_{555}	Green	0.88	0.03*	2.1541e + 3
Rrs_{645}	Red	0.59	0.09	2.1542e + 3
Rrs_{667}	Red	0.52	0.11	2.1542e + 3
Rrs_{678}	Red	0.35	0.16	2.1542e + 3

5. Conclusions

Our study evaluated the spatio-temporal trends in remote sensing reflectance (R_{rs}) along the inner sea of Chiloé (ISC) in the Chilean northern Patagonia. As with previous studies, the ISC was divided in northern and southern basins, due to their distinct oceanographic characteristics. Based on a large dataset (2003—2021) of R_{rs} collected by MODIS-Aqua, we observed marked seasonal patterns in all R_{rs} bands. When considering the spatial scales, the individual R_{rs} heterogeneity reveals negative and significant trends predominantly in the blue spectrum

(412, 443, 469, and 488). The trends in the band ratios between the green and blue bands (i.e., 469, 488, 531, 547, and 555 nm) allowed us to make inferences concerning the seasonality of river freshwater input, with elevated terrestrial suspended particulate and dissolved concentrations. It is essential to have a baseline for studying the trophic status of an inland marine system based on bio-optical properties (Potes et al., 2012; Turner et al., 2021). Future efforts require having *in situ* reflectance spectra of inland waters to identify environmental changes with high resolution (spatial, temporal, and spectral). This study reinforces that satellite data is a valuable complement to *in situ* measurements for the generation of regional algorithms to monitor water quality in northern Patagonia.

Declaration of Competing Interest

The authors declare that they have no known competing financial interests or personal relationships that could have appeared to influence the work reported in this paper.

Acknowledgments

C.L. acknowledge funding by FONDECYT 1230420 and Dirección de Investigación at the Universidad Católica de la Santísima Concepción FAA 2024. R.P.F. is supported by FONDECYT grant 1231494 and Centro de Investigación para la Gestión Integrada del Riesgo de Desastres (CIGIDEN), 1523A0009 FONDAP 2023. R.M. and S.I.V. were supported by the Chilean National Research and Development Agency (ANID) with the doctoral grant 21231834 and 21221020, respectively. G.S.S. is supported by FONDECYT grant 1220167 and COPAS Coastal ANID FB210021. I.P.S was funded by COPAS COASTAL ANID FB210021 and FONDECYT 1211037. B.R.B. is supported by FONDECYT 1221699. I.C. was funded by the Grant CNS2023-143630 funded by MICIU/AEI/10.13039/501100011033 and by European Union Next Generation EU/PRTR. This work represents a contribution to the CSIC Thematic Interdisciplinary Platforms PTI TELEDETECT and PTI OCEANS+. Finally, we thank Observatorio Marino Reloncavi (OMARE), Centro i-mar for the turbidity and chlorophyll-a data used in climatology.

Appendix A. Supplementary material

Supplementary data associated with this article can be found, in the online version, at https://doi.org/10.1016/j.asr.2024.11.014.

References

Aguayo, R., León-Muñoz, J., Garreaud, R., et al., 2021. Hydrological droughts in the southern andes (40–45 s) from an ensemble experiment using cmip5 and cmip6 models. Scient. Rep. 11 (1), 5530.

Ahmad, Z., Franz, B.A., McClain, C.R., et al., 2010. New aerosol models for the retrieval of aerosol optical thickness and normalized water-leaving radiances from the Seawifs and MODIS sensors over coastal regions and open oceans. Appl. Opt. 49 (29), 5545–5560.

Behrenfeld, M.J., 2014. Climate-mediated dance of the plankton. Nat. Clim. Change 4 (10), 880–887.

Behrenfeld, M.J., Westberry, T.K., Boss, E., et al., 2009. Satellite-detected fluorescence reveals global physiology of ocean phytoplankton. Biogeosciences 6 (5), 779–794.

Bisson, K., Boss, E., Werdell, P.J., et al., 2021. Seasonal bias in global ocean color observations. Appl. Opt. 60 (23), 6978–6988.

Blondeau-Patissier, D., Gower, J.F., Dekker, A.G., et al., 2014. A review of ocean color remote sensing methods and statistical techniques for the detection, mapping and analysis of phytoplankton blooms in coastal and open oceans. Prog. Oceanogr. 123, 123–144.

Cannizzaro, J.P., Carlson Jr, P.R., Yarbro, L.A., et al., 2013. Optical variability along a river plume gradient: Implications for management and remote sensing. Estuar. Coast. Shelf Sci. 131, 149–161.

Chen, Z., Hu, C., Muller-Karger, F., 2007. Monitoring turbidity in Tampa Bay using MODIS/Aqua 250-m imagery. Remot Sens. Environ. 109 (2), 207–220.

Cloern, J.E., 1987. Turbidity as a control on phytoplankton biomass and productivity in estuaries. Cont. Shelf Res. 7 (11–12), 1367–1381.

Constantin, S., Doxaran, D., Constantinescu, t., 2016. Estimation of water turbidity and analysis of its spatio-temporal variability in the danube river plume (black sea) using modis satellite data. Cont. Shelf Res. 112, 14–30.

Cuevas, L.A., Tapia, F.J., Iriarte, J.L., et al., 2019. Interplay between freshwater discharge and oceanic waters modulates phytoplankton size-structure in fjords and channel systems of the chilean patagonia. Prog. Oceanogr. 173, 103–113.

Cui, T., Zhang, J., Wang, K., et al., 2020. Remote sensing of chlorophyll a concentration in turbid coastal waters based on a global optical water classification system. ISPRS J. Photogram. Remote Sens. 163, 187–201.

Curra-Sánchez, E.D., Lara, C., Cornejo-D'Ottone, M., et al., 2022. Contrasting land-uses in two small river basins impact the colored dissolved organic matter concentration and carbonate system along a river-coastal ocean continuum. Sci. Total Environ. 806, 150435.

Demarcq, H., Noyon, M., Roberts, M.J., 2020. Satellite observations of phytoplankton enrichments around seamounts in the south west indian ocean with a special focus on the walters shoal. Deep Sea Res. Part II 176, 104800.

Dogliotti, A.I., Ruddick, K., Nechad, B., et al., 2015. A single algorithm to retrieve turbidity from remotely-sensed data in all coastal and estuarine waters. Remote Sens. Environ. 156, 157–168.

Doxaran, D., Babin, M., Leymarie, E., 2007. Near-infrared light scattering by particles in coastal waters. Opt. Express 15 (20), 12834–12849.

Dutkiewicz, S., Hickman, A.E., Jahn, O., et al., 2019. Ocean colour signature of climate change. Nat. Commun. 10 (1), 578.

Feldman, G., & McClain, C. (2014). Ocean Color Web.–SeaWiFS Reprocessing 2010.0, MODIS-Terra Reprocessing 2013.0, MODIS-Aqua Reprocessing 2013.1, VIIRS-SNPP Reprocessing 2014.0. NASA Goddard Space Flight Center/Eds. N. Kuring, SW Bailey. NASA Goddard Space Flight Center, Eds. N. Kuring, SW Bailey, http://oceancolor. gsfc. nasa. gov/(Access-October, 2015).

Flores, R.P., Lara, C., Saldías, G.S., et al., 2022. Spatio-temporal variability of turbid freshwater plumes in the Inner Sea of Chiloé, northern Patagonia. J. Mar. Syst., 103709

Franz, B.A., Werdell, P.J., Meister, G. et al. (2006). Modis land bands for ocean remote sensing applications. In Proc. Ocean Optics XVIII, Montreal, Canada (pp. 9–13). volume 10.

Friedland, K.D., Mouw, C.B., Asch, R.G., et al., 2018. Phenology and time series trends of the dominant seasonal phytoplankton bloom across global scales. Glob. Ecol. Biogeogr. 27 (5), 551–569.

García-Tuñon, W., Curra-Sánchez, E.D., Lara, C., et al., 2024. Spatio-temporal variability of turbidity derived from sentinel-2 in reloncaví sound, northern patagonia, chile. Ecol. Inform., 102814

Gilerson, A., Herrera-Estrella, E., Foster, R., et al., 2022. Determining the primary sources of uncertainty in retrieval of marine remote sensing reflectance from satellite ocean color sensors. Front. Remote Sens. 3, 25.

Gitelson, A.A., Gao, B.-C., Li, R.-R., et al., 2011. Estimation of chlorophyll-a concentration in productive turbid waters using a hyperspectral imager for the coastal ocean—the azov sea case study. Environ. Res. Lett. 6 (2), 024023.

Gitelson, A.A., Gurlin, D., Moses, W.J., et al., 2009. A bio-optical algorithm for the remote estimation of the chlorophyll-a concentration in case 2 waters. Environ. Res. Lett. 4 (4), 045003.

Gong, W., Browne, J., Hall, N., et al., 2017. Molecular insights into a dinoflagellate bloom. The ISME Journal 11 (2), 439–452.

González, H., Calderón, M., Castro, L., et al., 2010. Primary production and plankton dynamics in the Reloncaví Fjord and the Interior Sea of Chiloé, Northern Patagonia, Chile. Mar. Ecol. Prog. Ser. 402, 13–30.

González, H.E., Nimptsch, J., Giesecke, R., et al., 2019. Organic matter distribution, composition and its possible fate in the chilean north-patagonian estuarine system. Sci. Total Environ. 657, 1419–1431.

Hays, G.C., Richardson, A.J., Robinson, C., 2005. Climate change and marine plankton. Trends Ecol. Evol. 20 (6), 337–344.

Hellweger, F., Schlosser, P., Lall, U., et al., 2004. Use of satellite imagery for water quality studies in new york harbor. Estuar. Coast. Shelf Sci. 61 (3), 437–448.

Iriarte, J., González, H., Liu, K., et al., 2007. Spatial and temporal variability of chlorophyll and primary productivity in surface waters of southern chile (41.5–43 s). Estuar. Coast. Shelf Sci. 74 (3), 471–480.

Iriarte, J., León-Muñoz, J., Marcé, R., et al., 2017. Influence of seasonal freshwater streamflow regimes on phytoplankton blooms in a patagonian fjord. NZ J. Mar. Freshwat. Res. 51 (2), 304–315.

Karimi, B., Hashemi, S.H., Aghighi, H., 2024. Application of landsat-8 and sentinel-2 for retrieval of chlorophyll-a in a shallow freshwater lake. Adv. Space Res.

Katsaros, K.B. (2015). An introduction to ocean remote sensing, 2?? ed.

Laiolo, L., Matear, R., Soja-Woźniak, M., et al., 2021. Modelling the impact of phytoplankton cell size and abundance on inherent optical properties (iops) and a remotely sensed chlorophyll-a product. J. Mar. Syst. 213, 103460.

Lara, C., Saldías, G.S., Tapia, F.J., et al., 2016. Interannual variability in temporal patterns of chlorophyll–a and their potential influence on the supply of mussel larvae to inner waters in northern Patagonia (41–44° S). J. Mar. Syst. 155, 11–18.

Lee, Z., Carder, K., Arnone, R., et al., 2007. Determination of primary spectral bands for remote sensing of aquatic environments. Sensors 7 (12), 3428–3441.

León-Muñoz, J., Aguayo, R., Marcé, R. et al. (2021). Climate and land cover trends affecting freshwater inputs to a fjord in northwestern Patagonia. Frontiers in Marine Science, (p. 960).

León-Muñoz, J., Echeverría, C., Marcé, R., et al., 2013. The combined impact of land use change and aquaculture on sediment and water quality in oligotrophic lake Rupanco (north Patagonia, Chile, 40.8°S). J. Environ. Manage. 128, 283–291.

Linford, P., Pérez-Santos, I., Montes, I., et al., 2023. Recent deoxygenation of patagonian fjord subsurface waters connected to the peru–chile undercurrent and equatorial subsurface water variability. Global Biogeochem. Cycles (p. e2022GB007688).

Liu, G., Li, L., Song, K., et al., 2020. An olci-based algorithm for semi-empirically partitioning absorption coefficient and estimating chlorophyll a concentration in various turbid case-2 waters. Remote Sens. Environ. 239, 111648.

Lo Prejato, M., McKee, D., Mitchell, C., 2020. Inherent optical properties-reflectance relationships revisited. J. Geophys. Res.: Oceans 125 (11), e2020JC016661.

Mann, K.H., Lazier, J.R., 2005. Dynamics of marine ecosystems: biological-physical interactions in the oceans. John Wiley & Sons.

McKinna, L.I., Cetinić, I., Werdell, P.J., 2021. Development and validation of an empirical ocean color algorithm with uncertainties: a case study with the particulate backscattering coefficient. J. Geophys. Res.: Oceans 126 (5), e2021JC017231.

Menken, K.D., Brezonik, P.L., Bauer, M.E., 2006. Influence of chlorophyll and colored dissolved organic matter (cdom) on lake reflectance spectra: Implications for measuring lake properties by remote sensing. Lake and Reservoir Manage. 22 (3), 179–190.

Menon, H.B., Adhikari, A., 2018. Remote sensing of chlorophyll-a in case II waters: A novel approach with improved accuracy over widely implemented turbid water indices. J. Geophys. Res.: Oceans 123 (11), 8138–8158.

Mishra, S., Mishra, D.R., 2012. Normalized Difference Chlorophyll index: A novel model for remote estimation of chlorophyll-a concentration in turbid productive waters. Remote Sens. Environ. 117, 394–406.

Morel, A., Berthon, J.-F., 1989. Surface pigments, algal biomass profiles, and potential production of the euphotic layer: Relationships reinvestigated in view of remote-sensing applications. Limnol. Oceanogr. 34 (8), 1545–1562.

Morel, A., Prieur, L., 1977. Analysis of variations in ocean color 1. Limnol. Oceanogr. 22 (4), 709–722.

Muñoz, R., Lara, C., Arteaga, J., et al., 2023. Temporal synchrony in satellite-derived ocean parameters in the inner sea of chiloé, northern patagonia, chile. Remote Sensing 15 (8), 2182.

Nasiha, H.J., Wang, Z., Giannini, F., et al., 2022. Spatial variability of in situ above-water reflectance in coastal dynamic waters: implications for satellite match-up analysis. Front. Remote Sens. 3, 876748.

Nechad, B., Ruddick, K., Neukermans, G., 2009. Calibration and validation of a generic multisensor algorithm for mapping of turbidity in coastal waters. In: Remote Sensing of the Ocean, Sea Ice, and Large Water Regions 2009, pp. 161–171, SPIE volume 7473.

O'Reilly, J.E., Maritorena, S., Mitchell, B.G., et al., 1998. Ocean color chlorophyll algorithms for seawifs. J. Geophys. Res.: Oceans 103 (C11), 24937–24953.

Pahlevan, N., Smith, B., Schalles, J., et al., 2020. Seamless retrievals of chlorophyll-a from sentinel-2 (msi) and sentinel-3 (olci) in inland and coastal waters: A machine-learning approach. Remote Sens. Environ. 240, 111604.

Potes, M., Costa, M.J., Salgado, R., 2012. Satellite remote sensing of water turbidity in alqueva reservoir and implications on lake modelling. Hydrol. Earth Syst. Sci. 16 (6), 1623–1633.

Roy, S., Llewellyn, C.A., Egeland, E.S., et al., 2011. Phytoplankton pigments: characterization, chemotaxonomy and applications in oceanography. Cambridge University Press.

Saberioon, M., Brom, J., Nedbal, V., et al., 2020. Chlorophyll-a and total suspended solids retrieval and mapping using sentinel-2a and machine learning for inland waters. Ecol. Ind. 113, 106236.

Saldías, G.S., Hernández, W., Lara, C., et al., 2021. Seasonal variability of sst fronts in the inner sea of chiloé and its adjacent coastal ocean, northern patagonia. Remote Sensing 13 (2), 181.

Sapiano, M., Brown, C., Schollaert Uz, S., et al., 2012. Establishing a global climatology of marine phytoplankton phenological characteristics. J. Geophys. Res.: Oceans 117 (C8).

Sherman, J., Tzortziou, M., Turner, K.J., et al., 2023. Chlorophyll dynamics from sentinel-3 using an optimized algorithm for enhanced ecological monitoring in complex urban estuarine waters. Int. J. Appl. Earth Obs. Geoinf. 118, 103223.

Shi, W., Wang, M., 2019. A blended inherent optical property algorithm for global satellite ocean color observations. Limnol. Oceanogr.: Methods 17 (7), 377–394.

Strub, P.T., James, C., Montecino, V., et al., 2019. Ocean circulation along the southern chile transition region (38–46 s): Mean, seasonal and interannual variability, with a focus on 2014–2016. Prog. Oceanogr. 172, 159–198.

The MathWorks Inc. (2017). Matlab version: 9.3.0 (r2017b). URL: https://www.mathworks.com.

Tilstone, G.H., Pardo, S., Dall'Olmo, G., et al., 2021. Performance of ocean colour chlorophyll a algorithms for sentinel-3 olci, modis-aqua

and suomi-viirs in open-ocean waters of the atlantic. Remote Sens. Environ. 260, 112444.
Topp, S.N., Pavelsky, T.M., Jensen, D., et al., 2020. Research trends in the use of remote sensing for inland water quality science: Moving towards multidisciplinary applications. Water 12 (1), 169.
Trombetta, T., Vidussi, F., Mas, S., et al., 2019. Water temperature drives phytoplankton blooms in coastal waters. PloS one 14 (4), e0214933.
Turner, J.S., Friedrichs, C.T., Friedrichs, M.A., 2021. Long-term trends in chesapeake bay remote sensing reflectance: Implications for water clarity. J. Geophys. Res.: Oceans 126 (12), e2021JC017959.
Vargas, C.A., Martinez, R.A., San Martin, V., et al., 2011. Allochthonous subsidies of organic matter across a lake–river–fjord landscape in the chilean patagonia: implications for marine zooplankton in inner fjord areas. Cont. Shelf Res. 31 (3–4), 187–201.
Vásquez, S.I., de la Torre, M.B., Saldías, G.S., et al., 2021. Meridional changes in satellite chlorophyll and fluorescence in optically-complex coastal waters of northern patagonia. Remote Sensing 13 (5), 1026.
Wang, Y., Wu, H., Lin, J., et al., 2019. Phytoplankton blooms off a high turbidity estuary: a case study in the changjiang river estuary. J. Geophys. Res.: Oceans 124 (11), 8036–8059.
Wei, J., Lee, Z., Garcia, R., et al., 2018. An assessment of landsat-8 atmospheric correction schemes and remote sensing reflectance products in coral reefs and coastal turbid waters. Remote Sens. Environ. 215, 18–32.
Werdell, P.J., McKinna, L.I., Boss, E., et al., 2018. An overview of approaches and challenges for retrieving marine inherent optical properties from ocean color remote sensing. Prog. Oceanogr. 160, 186–212.
Werther, M., Odermatt, D., Simis, S.G., et al., 2022. Characterising retrieval uncertainty of chlorophyll-a algorithms in oligotrophic and mesotrophic lakes and reservoirs. ISPRS J. Photogram. Remote Sens. 190, 279–300.
Wetz, M.S., Hales, B., Chase, Z., et al., 2006. Riverine input of macronutrients, iron, and organic matter to the coastal ocean off oregon, usa, during the winter. Limnol. Oceanogr. 51 (5), 2221–2231.
Winder, M., Sommer, U., 2012. Phytoplankton response to a changing climate. Hydrobiologia 698, 5–16.
Yang, H., Kong, J., Hu, H., et al., 2022. A review of remote sensing for water quality retrieval: progress and challenges. Remote Sens. 14 (8), 1770.